

FIG. 1: Upper panel: Pictorial representation of the cut-and-paste technique. The original communication channel \mathcal{M} is entanglement breaking. By dividing it in smaller sections represented by the maps $\Phi_1, \Phi_2, \Phi_3, \Phi_4$ and recombining them in a proper order we construct a new communication line \mathcal{M}' which is less noisy than the original one, in particular it is not entanglement breaking. Lower panel: merging of two spatially homogeneous EB channels \mathcal{M}_1 and \mathcal{M}_2 to form the non EB map \mathcal{M}' .

$n = 1, \dots, N$, Φ_n is the transformation which propagates the messages on the n -th section of the line. Now assume that \mathcal{M} is EB: accordingly it will prevent the transferring of any form of quantum correlations. Yet, in what follows we are going to show that there are cases where, by simply reshuffling the order in which the sub-channels are connected with each other, we can create a new physical map $\mathcal{M}' = \Phi_{i_N} \circ \Phi_{i_{N-1}} \circ \dots \circ \Phi_{i_2} \circ \Phi_{i_1}$ that doesn't suffer from such limitations (i_1, i_2, \dots, i_N being a permutation of the first N natural numbers). An interesting application of this effect is presented in the lower panel of Fig. 1. Here we are in the presence of two communication lines, \mathcal{M}_1 and \mathcal{M}_2 , of length L_1 and L_2 respectively, which are both EB and which, for the sake of simplicity, we assume to be spatially homogeneous. As we shall see in the next sections, there are situations in which we can create a new communication line \mathcal{M}_3 which allows one to reliably propagate quantum coherence over distances L_3 much larger than $L_1 + L_2$, by simply alternating pieces of the original maps i.e.

$$\mathcal{M}_3 = (\Phi \circ \Psi) \circ (\Phi \circ \Psi) \circ \dots \circ (\Phi \circ \Psi) \notin \text{EB} \quad (1)$$

with Φ (resp. Ψ) being the sub-channel that composes \mathcal{M}_1 (resp. \mathcal{M}_2) – the maximum value of L_3 being a function of the size of the pieces we have selected.

The cut-and-paste effect detailed above ultimately relies on the non-commutative character of quantum mechanics, where it is not just the kind of operations performed on a system that matters, but also the order in which they are carried on. At variance with previous applications, here such peculiar aspect of the the-

ory exhibits its full potential impact, by allowing or not allowing a well defined operational task (i.e. the sharing of entanglement among distant parties). On a more practical ground, our results can find applications in the realization of quantum networks connected by highly damping and noisy communication links. More generally they suggest a new way of engineering quantum devices, widening the possibilities of optimising their performances by simply reordering the elements which constitute them.

In what follows we review some basic facts about EB maps and discuss the cut-and-paste mechanism by focusing on two examples: the first regards amplitude damping and phase damping channels operating on a qubit [3]; the second instead deals with a continuous model in which the propagation of signals in a noisy environment is represented in terms of effective master equations. Then for the amplitude damping example we present an experimental test of this effect where the qubits are encoded into the polarization degree of freedom of single photons.

II. THEORETICAL ANALYSIS

A quantum channel Φ is said to be EB if, when applied to one part of an entangled state, the output is always separable for every choice of the input [14]. Moreover it can be shown that $\Phi \in \text{EB}$ if and only if, when operating locally on the system of interest S , it turns a maximally entangled state $|\Omega\rangle_{SA}$ of S and of an ancillary system A , into a separable one [14], i.e.:

$$\rho_{SA}^{(\text{out})} = (\Phi \otimes \mathbb{I})(|\Omega\rangle_{SA}\langle\Omega|) \text{ is separable} \iff \Phi \in \text{EB}, \quad (2)$$

with \mathbb{I} being the identity channel operating on A . A possible way to smooth the boundary between these “bad” kind of channels and the “good” non-EB channels, is the notion of EB *order* of a channel introduced in [27], and further studied in [28]. Accordingly Φ is said to be EB of order n if it requires n consecutive applications to destroy the entanglement of any input state, i.e. if up to $n - 1$ iterations of Φ are not EB, while n (or more) iterations of Φ yields a EB transformation.

A. Cut-and-paste with discrete maps

Amplitude Damping (AD) channels are an important class of maps acting on a qubit [3]. They describe dissipation and decoherence processes of a two-level system in thermal contact with a zero temperature external bath, or the loss of a photon in the propagation of single photon pulses along an optical fiber. Given an input density matrix ρ the channel \mathcal{A}_η transforms it as $\mathcal{A}_\eta(\rho) \equiv E_1\rho E_1^\dagger + E_2\rho E_2^\dagger$, where $E_1 \equiv \begin{bmatrix} 1 & 0 \\ 0 & \sqrt{\eta} \end{bmatrix}$ and

$E_2 \equiv \begin{bmatrix} 0 & \sqrt{1-\eta} \\ 0 & 0 \end{bmatrix}$, are the Kraus operators expressed in the computational basis of the qubit, and $\eta \in [0, 1]$ is the transmission coefficient characterizing the map, interpolating between perfect transmission $\eta = 1$ and complete damping $\eta = 0$. One can easily verify that \mathcal{A}_η is never EB for $\eta > 0$ and, from the semigroup property

$$\mathcal{A}_{\eta_2} \circ \mathcal{A}_{\eta_1} = \mathcal{A}_{\eta_1} \circ \mathcal{A}_{\eta_2} = \mathcal{A}_{\eta_2 \eta_1}, \quad (3)$$

that it also has infinite order, i.e. $n = \infty$. Interestingly enough however, it can be shown [27] that for sufficiently small values of the transmission coefficient η , the order of \mathcal{A}_η can be reduced by post-posing or ante-posing suitable unitary gates. In particular one can identify (non-unique) unitary operations $\rho \rightarrow \mathcal{U}(\rho) = U\rho U^\dagger$ such that the channels

$$\Phi = \mathcal{A}_\eta \circ \mathcal{U}, \quad \Psi = \mathcal{U}^\dagger \circ \mathcal{A}_\eta, \quad (4)$$

are both EB of order $n = m = 2$: for instance this happens at $\eta = 0.3$ when we take the bit-flip σ_x as U . What it is more interesting, we can now use these maps to provide a first evidence of the cut-and-paste mechanism. Indeed consider the compound map \mathcal{M} formed by two applications of Φ and followed by two applications of Ψ , i.e. $\mathcal{M} = \Phi \circ \Phi \circ \Psi \circ \Psi$ (corresponding to set $\Phi_1 = \Phi_2 = \Phi$ and $\Phi_3 = \Phi_4 = \Psi$ in the upper panel of Fig. 1). This is clearly EB, however the alternate application of the two maps produces the AD channel of transmissivity η^4 which, as already stated, is never EB:

$$\begin{aligned} \mathcal{M}' &= \Phi \circ \Psi \circ \Phi \circ \Psi \\ &= \mathcal{A}_\eta \circ \mathcal{U} \circ \mathcal{U}^\dagger \circ \mathcal{A}_\eta \circ \mathcal{A}_\eta \circ \mathcal{U} \circ \mathcal{U}^\dagger \circ \mathcal{A}_\eta = \mathcal{A}_{\eta^4} \notin \text{EB}. \end{aligned} \quad (5)$$

Similar results can also be obtained by replacing in the above expressions the AD map \mathcal{A}_η with the phase-damping (PD) channel \mathcal{E}_p [3]. For $p \in [0, 1]$ the latter transforms a generic input density matrix ρ of the qubit as $\mathcal{E}_p(\rho) \equiv 1/2((1+p)\rho + (1-p)\sigma_z\rho\sigma_z)$ describing loss of coherence between its energy eigenstates. Analogously to the AD maps, $\mathcal{E}_p \notin \text{EB}$ for $p > 0$ and satisfies the semigroup property $\mathcal{E}_{p_2} \circ \mathcal{E}_{p_1} = \mathcal{E}_{p_1} \circ \mathcal{E}_{p_2} = \mathcal{E}_{p_2 p_1}$, from which it immediately follows that they are EB of infinite order, i.e. $\mathcal{E}_p \in \text{EB}^n$ for $n = \infty$. Furthermore also in this case for p sufficiently small one can find a unitary transformation \mathcal{U} such that the maps $\Phi = \mathcal{E}_p \circ \mathcal{U}$ and $\Psi = \mathcal{U}^\dagger \circ \mathcal{E}_p$ are EB of order 2, e.g. by fixing $p = 0.4$ and $U = 1/\sqrt{2}(\sigma_z - \sigma_x)$.

The examples presented here constitute also a clear ‘‘proof of principle’’ demonstration of the merging effect described in the lower panel of Fig. 1. Indeed both in the AD and in the PD implementation, not only the channel \mathcal{M} is EB, but also the maps associated with its first and second sections (i.e. the maps $\mathcal{M}_1 = \Phi \circ \Phi$ and $\mathcal{M}_2 = \Psi \circ \Psi$ respectively) share the same property. Yet even though individually such transformations are both bad operations, when split and merged as in (5) they manage to somehow correct their detrimental effects. This is a curious instance of an effective quantum error

correction procedure obtained by properly mixing two different types of errors. Furthermore, due to their semigroup property which both the AD and PD maps fulfil, the channel $\Phi \circ \Psi$ has actually an infinite order ($n = \infty$). Accordingly the procedure can be iterated an arbitrary number of times obtaining an infinitely long sequence $(\Phi \circ \Psi) \circ (\Phi \circ \Psi) \circ \dots$ which nonetheless can still transmit a non-zero fraction of entanglement (corresponding to have a divergent value of L_3 of Fig. 1).

B. Cut-and-paste with continuous channels

The potentiality of the cut-and-paste method is much more general and is not restricted to idealized sequences of discrete unitary and dissipative operations discussed so far. In more realistic scenarios, like the continuous propagation of a quantum state along a physical medium, the transmission is better described by continuous homogeneous channels (also known as quantum dynamical semigroups) [29, 30]. In this framework, the propagation of a signal for an infinitesimal distance dx , induces a change of the density matrix according to a master equation of the form:

$$\frac{d\rho}{dx} = \mathcal{L}(\rho), \quad (6)$$

where the linear Liouvillian operator \mathcal{L} , completely characterizes the channel and generates simultaneously the unitary and dissipative dynamics of the system [29, 30]. The formal solution of Eq. (6), is $\rho(x) = e^{\mathcal{L}x}\rho(0)$ and represents the propagation of the quantum state for a finite length x along the physical medium.

Now, as in the case of the lower panel of Fig. 1, assume that we have at disposal two of these maps (e.g. two different wave guides) characterized by \mathcal{L}_1 and \mathcal{L}_2 , such that the integrated dynamics becomes EB after a propagation length of $x = L_1$ and $x = L_2$ respectively, i.e. :

$$\mathcal{M}_1 = e^{\mathcal{L}_1 L_1} \in \text{EB}, \quad \mathcal{M}_2 = e^{\mathcal{L}_2 L_2} \in \text{EB}. \quad (7)$$

If we divide the two transmission lines into shorter pieces of length L_1/n_1 and L_2/n_2 we, obtain the following maps $\Phi = e^{\mathcal{L}_1 L_1/n_1}$ and $\Psi = e^{\mathcal{L}_2 L_2/n_2}$, which are, by construction, EB of order n_1 and n_2 . The idea is thus to construct a new communication line using Φ and Ψ as elementary building blocks which are merged to form an alternate sequence as in Eq. (1) with the aim of increasing the entanglement propagation length as much as possible. As an example we can consider two hypothetical transmission lines, characterized by the following Liouvillian operators [29, 30]:

$$\mathcal{L}_j(\rho) = -i[H_j, \rho] + \frac{\epsilon}{2}(2\sigma_- \rho \sigma_+ - \sigma_+ \sigma_- \rho - \rho \sigma_+ \sigma_-), \quad (8)$$

where $j = 1, 2$, $H_1 = \Omega\sigma_x$, $H_2 = -\Omega\sigma_x$ and $\sigma_\pm = (\sigma_x \pm i\sigma_y)/2$. The first term in this equation induces a

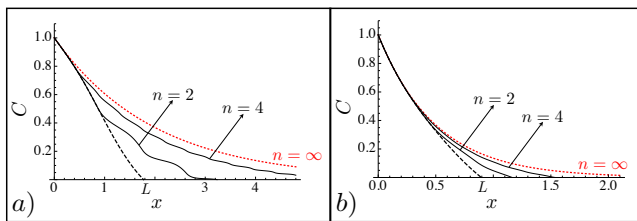


FIG. 2: Residual concurrence [31] as a function of the propagation distance x for different continuous channels. At $x = 0$ the system is initialized in the singlet state. Panel a) refers to the rotating amplitude damping channels defined in Eq. (8) (black dashed line) and their associated cut-and-paste improvements described in Eq. (9) for different values of n (black lines). The limit for $n \rightarrow \infty$ is also represented (red dotted line). Panel b) instead is based on the rotating phase damping channels defined in Eq. (10), while the notation is the same as for panel a). The values of the parameters are $\Omega = 1.5$ and $\epsilon = 1$ for both subfigures which yield $L = 1.75$ for Eq. (8) and $L = 0.85$ for Eq. (10) for the maximum propagation length that allow for quantum coherence preservation (beyond these values the maps become EB). The cut-and-paste approach allows to significantly increase the EB threshold well beyond the original one: for instance in the case of Eq. (8) setting $n = 2$ already gives L_3 which is more than twice the value of L (similarly this happens also for the case of Eq. (10) by setting $n = 4$).

unitary rotation of the quantum state while the second term is responsible for the dissipative dynamics. Accordingly Eq. (8) is a sort of continuous analogue of the discrete maps of Eq. (4) where the two different form of transformations (i.e. \mathcal{A}_η and \mathcal{U}) are applied to the system not one after the other but simultaneously.

For nonzero values of Ω and ϵ , both channels become EB at the same finite propagation length L . For simplicity we cut slices of equal length L/n for both channels, and we paste them according to the alternating sequence given in Eq. (1). This new continuous channel is formally described by a master equation in which the Liouvillian operator switches between \mathcal{L}_1 and \mathcal{L}_2 after the propagation of L/n space intervals, *i.e.*

$$\frac{d\rho}{dx} = \mathcal{L}_3^{(n)}(\rho) = \begin{cases} \mathcal{L}_1(\rho), & \text{for } \lfloor \frac{x}{L/n} \rfloor = \text{even}, \\ \mathcal{L}_2(\rho), & \text{for } \lfloor \frac{x}{L/n} \rfloor = \text{odd}, \end{cases} \quad (9)$$

where $\lfloor \cdot \rfloor$ is the integer part of the argument.

We now test the entanglement condition given in Eq. (2), *i.e.* we study the entanglement evolution induced by the channel $\mathcal{L}_3^{(n)}$ when applied to one part of a maximally entangled state. The value of entanglement measured in terms of the concurrence [31] as a function of the distance x is represented in Fig. 2a for different values of n . We observe that with respect to the original channels \mathcal{L}_1 and \mathcal{L}_2 , the new channels $\mathcal{L}_3^{(n)}$ become entanglement breaking at larger distances. Moreover, the entanglement propagation length increases with n , and tends to infinity. This

fact can be proved theoretically: using a simple Trotter decomposition argument, the dynamics for $n \rightarrow \infty$ tends to a pure amplitude damping channel which is never entanglement breaking.

Exactly the same analysis and similar results are valid also for other continuous channels. For example if we replace equation (8) with

$$\mathcal{L}_j(\rho) = -i[H_j, \rho] + \frac{\epsilon}{2}[\sigma_z, [\sigma_z, \rho]], \quad (10)$$

we obtain two propagation media indexed by $j = 1, 2$ in which a qubit is rotated in different directions by $H_1 = \Omega\sigma_x$ and $H_2 = -\Omega\sigma_x$ while, at the same time, it is subject to a dephasing process [29, 30]. Remarkably, this is a quite realistic model for the propagation polarization qubits in optical fibers, in which dephasing and polarization drift can simultaneously affect the transmitted photons. Fig. 2b demonstrates that our approach is applicable also in this situation, obtaining a significant enhancement of the entanglement propagation distance.

III. EXPERIMENTAL IMPLEMENTATION

In this section we present a quantum optics experiment demonstrating the possibility of restoring the transmission of entanglement via the cut-and-paste technique previously described. Specifically we study the transmission of a qubit encoded in the horizontal and vertical polarization of a photon $\{|0\rangle \equiv |H\rangle, |1\rangle \equiv |V\rangle\}$ and, inspired by Eq. (4), we take

$$\Phi = \mathcal{A}_{\eta_2} \circ \mathcal{U}_\theta, \quad \Psi = \mathcal{U}_\varphi \circ \mathcal{A}_{\eta_1}, \quad (11)$$

where now the unitary mappings \mathcal{U}_ξ with $\xi = \theta, \varphi$ induce the rotation $U_\xi \equiv \begin{bmatrix} \cos(2\xi) & \sin(2\xi) \\ \sin(2\xi) & -\cos(2\xi) \end{bmatrix}$ in the polarization degree of freedom of the photon.

The experimental setting is sketched in Fig. 3: for assigned values of η_1, η_2, θ and φ , it is designed to study the presence/absence of entanglement on a maximally polarization entangled state $|\Omega\rangle_{SA}$ of a two-photon pair, which evolves under the transformation (2) given by the channels $\mathcal{M}' = \Phi \circ \Psi \circ \Phi \circ \Psi$, $\mathcal{M}_1 = \Phi \circ \Phi$, or $\mathcal{M}_2 = \Psi \circ \Psi$ by properly tuning the parameters of the interferometer (see below for details). For each one of these three choices the EB character of the transformation is hence determined exploiting the equivalence (2) by measuring the concurrence [31] of the associated density matrix $\rho_{SA}^{(\text{out})}$ through full tomography performed at the output of the setup: evidence of the cut-and-paste effect is thus obtained whenever one notices a non-zero value for the concurrence for \mathcal{M}' in correspondence with a zero concurrence value for \mathcal{M}_1 and \mathcal{M}_2 .

In our test we employ as $|\Omega\rangle_{SA}$ the superpositions $(|H\rangle_S|V\rangle_A + e^{i\phi}|V\rangle_S|H\rangle_A)/\sqrt{2}$ created through a high-brilliance, high-purity polarization entanglement source (see [32]). The source consists of a nonlinear PPKTP

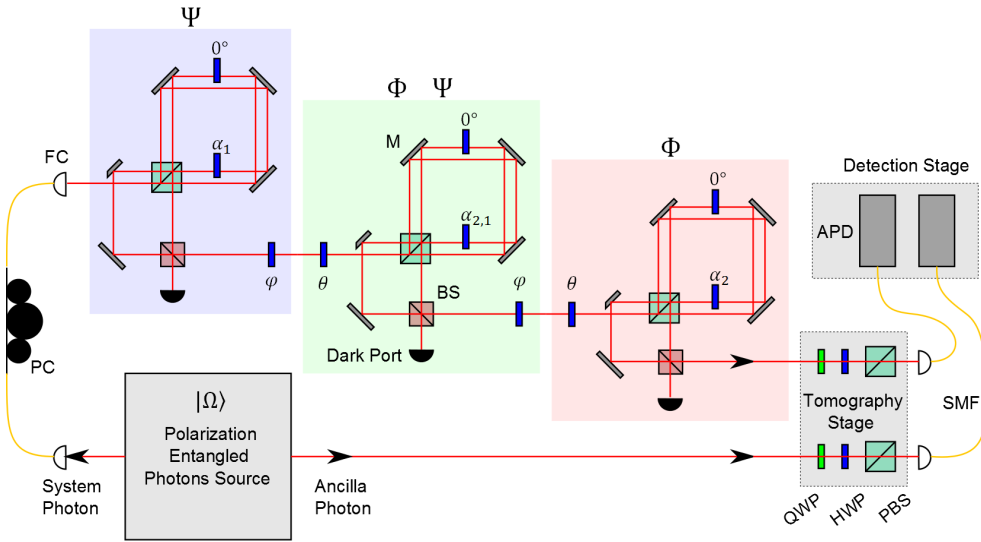


FIG. 3: Scheme of the experimental setup. The A photon belonging to the polarization entangled state $|\Omega\rangle_{SA}$ is directly linked to the detector, while the S photon is connected to the three DIF via a single-mode optical fiber (SMF). A bipartite full tomography stage, given by one HWP and one quarter wave plate (QWP) for both the system and the ancilla photons, allows to reconstruct the density matrix of the two-photon state. Finally, photons pairs are coupled to two electronically synchronized avalanche photodiodes (APDs) through two SMFs. PC: Polarization Controller. BS and PBS: Beam Splitter and Polarizing Beam Splitter.

crystal pumped by a single mode laser at $405nm$ and $2.75mW$ of power within a Sagnac Interferometer (SI), and able to generate pairs of photons in the system mode S and the ancillary mode A , at $810nm$ by Type-II parametric down conversion. The generated pairs (more than 50000 detected coincidences/sec) have a coherence length of $L_{coh} = 1.02mm$ and spectral bandwidth $\Delta\lambda = 0.43nm$. The ancillary photon A is hence directly transmitted to a detector station, while the photon S is connected to the testing area which implements the action of the maps \mathcal{M}' , \mathcal{M}_1 and \mathcal{M}_2 through both free-space and fiber optics links, and then sent to a second detector station, see Fig. 3.

When emerging from the source, the resulting state has more than 98% of fidelity with the target $|\Omega\rangle_{SA}$ and concurrence equal to $C = 0.98$, corresponding to an effective $C = 0.94$ at the interferometer detectors, because of the unavoidable entanglement degradation occurring in the connection with the testing channel (see Appendix B).

The mappings \mathcal{U}_ξ entering (11) are implemented by placing properly oriented Half-Wave Plates (HWP) along the optical axis of the propagating photons. The AD channels \mathcal{A}_{η_1} and \mathcal{A}_{η_2} are instead realized by means of a dual interferometric setup (DIF) obtained by putting two independent polarization controls inside a displaced SI, coupled to an external unbalanced Mach-Zehnder interferometer (MZI) (see Appendix A for more details on this).

To implement $\mathcal{M}' = \Phi \circ \Psi \circ \Phi \circ \Psi$ we exploit the semigroup property (3) to formally express the product $\mathcal{A}_{\eta_1} \circ \mathcal{A}_{\eta_2}$ as a single AD channel with damping parameter

$\eta_2\eta_1$. Accordingly we write

$$\mathcal{M}' = \mathcal{A}_{\eta_2} \circ \mathcal{U}_\theta \circ \mathcal{U}_\varphi \circ \mathcal{A}_{\eta_1\eta_2} \circ \mathcal{U}_\theta \circ \mathcal{U}_\varphi \circ \mathcal{A}_{\eta_1}. \quad (12)$$

This simple trick enables us to implement the whole transformation by means of three DIFs only instead of four (one for each AD map entering the original sequence), by taking the parameters α_1 , $\alpha_{2,1}$ and α_2 of Fig. 3 equal to $\arccos(-\sqrt{\eta_1})/2$, $\arccos(-\sqrt{\eta_2\eta_1})/2$, and $\arccos(-\sqrt{\eta_2})/2$, respectively (see Eq. (A2) of the Appendix A). For fixed values of η_2 and θ , the action of $\mathcal{M}_1 = \Phi \circ \Phi$ is studied by deactivating both Ψ maps in (12). Such operation is realized in two steps. First, the HWP placed in the internal vertically polarized path of the first DIF of Fig. 3 is set to $\alpha_1 = \pi/2$ to simulate $\eta_1 = 1$, while the HWPs placed in the internal vertically polarized paths of the second and third DIF, are set to induce the same rotation (i.e. $\alpha_{2,1} = \alpha_2 = \arccos(-\sqrt{\eta_2})/2$). Secondly, both the external HWPs of Fig. 3 which are responsible for the implementation of \mathcal{U}_φ are simply taken off from the setup. Similarly, for each given value of η_1 and φ , we can study the action of $\mathcal{M}_2 = \Psi \circ \Psi$ deactivating both Φ maps, by taking off from the setup both the external HWPs associated with the rotation \mathcal{U}_θ , and by letting the internal HWPs of the three DIFs as $\alpha_1 = \alpha_{2,1} = \arccos(-\sqrt{\eta_1})/2$ and $\alpha_2 = \pi/2$ to simulate $\eta_2 = 1$. Finally, the implementation of the identity channel (useful to directly measure the net entanglement of the input state available at the detectors of the interferometer) is obtained by setting $\alpha_1 = \alpha_{2,1} = \alpha_2 = \pi/2$ and removing all the external HWPs.

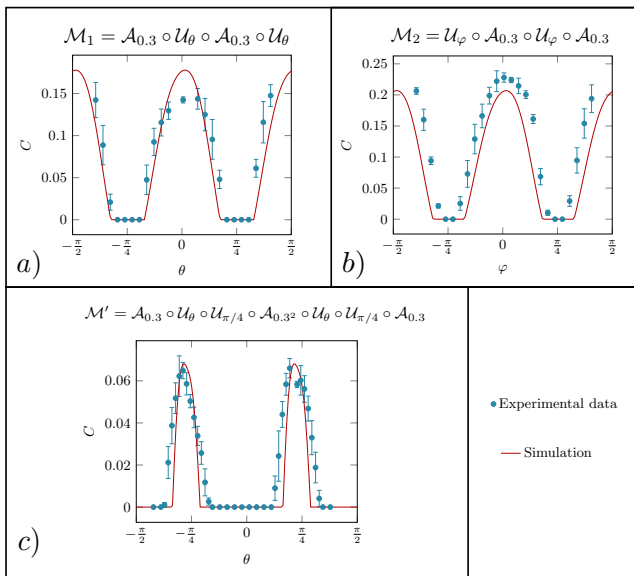


FIG. 4: Entanglement breaking analysis for the maps $\mathcal{M}_1 = \Phi \circ \Phi$, $\mathcal{M}_2 = \Psi \circ \Psi$ and $\mathcal{M}' = \Phi \circ \Psi \circ \Phi \circ \Psi$ obtained by cascading the channels of Eq. (11) with $\eta_1 = \eta_2 = 0.3$. a) Functional dependence upon the angle θ of the concurrence C of the state (2) at the output the channel \mathcal{M}_1 obtained from the scheme of Fig. 3 by setting $\alpha_1 = \pi/2$, $\alpha_{2,1} = \alpha_2 = \arccos(-\sqrt{\eta_2})/2$ and removing the rotations \mathcal{U}_φ (see text). For θ around $\pm\pi/4$ the system exhibits zero concurrence showing that the $\Phi \circ \Phi$ is EB, or equivalently that Φ is EB of order 2. b) Functional dependence upon the angle φ of the concurrence C of the state (2) at the output the channel \mathcal{M}_2 obtained by setting $\alpha_1 = \alpha_{2,1} = \arccos(-\sqrt{\eta_1})/2$ and $\alpha_2 = \pi/2$ and removing the rotations \mathcal{U}_θ . Similarly to the previous case, for φ around $\pm\pi/4$ the system exhibits zero concurrence showing that the $\Psi \circ \Psi$ is EB, or equivalently that Ψ is EB of order 2. c) Functional dependence upon the angle θ of the concurrence C of the state (2) at the output the channel \mathcal{M}' obtained by setting $\alpha_1 = \alpha_2 = \arccos(-\sqrt{0.3})/2$, $\alpha_{2,1} = \arccos(-0.3)/2$ and keeping $\varphi = \frac{\pi}{4}$. In all plots the red curves represents the theoretical prediction obtained by considering the actual experimental conditions (see Appendix B). Each point and the associated statistical error was taken from a set of N measurements ($3 \leq N \leq 11$), under equivalent mode coupling conditions.

In Fig. 4 we report the results obtained having set the transmission coefficients of the AD channels entering Eq. (11) at $\eta_1 = \eta_2 = 0.3$ (value for which we have already anticipated the possibility of witnessing the cut-and-paste effect). In particular panels a) and b) show the EB analysis for the maps $\mathcal{M}_1 = \Phi \circ \Phi$ and $\mathcal{M}_2 = \Psi \circ \Psi$ when, respectively, θ and φ are varied. In both cases one may notice that the concurrences of the associated SA output states (2) nullify when these angles reach the values $\pm\pi/4$, implying hence that under these conditions the channels Φ and Ψ are EB of order 2. Panel c) shows instead the EB analysis for the map \mathcal{M}' of Eq. (12) when the angle φ is kept constant at $\frac{\pi}{4}$ and θ is varied: one notices that the concurrence of the output state (2) is peaked and different from zero around

$\theta = \pm\pi/4$, indicating that for these values the map is not EB. Our data provide hence a clear experimental evidence of the cut-and-paste entanglement restoring effect for $\eta_1 = \eta_2 = 0.3$, $\theta = \pm\pi/4$, and $\varphi = \pm\pi/4$. The theoretical prediction corresponding to the red curves shown in the figure have been obtained by taking into account the actual optical elements of the experimental setup – the slight residual disagreement being mainly due to the unavoidable difficulties of coupling different polarization and path contributions within the same single mode fiber (see Appendix B for details).

IV. CONCLUSIONS

“Cutting” two entanglement-breaking channels into two or more pieces and properly reordering the corresponding parts can yield a new communication line which is not entanglement-breaking: this is the essence of the cut-and-paste protocol. In this work we give the first theoretical proposal both for discrete and continuous time evolution, the latter proving a more realistic model for signals evolution within a piece of material. We considered as benchmarks for a proof-of-principle demonstration the rotated amplitude and phase damping maps. In the second part of the manuscript, we focused on the discrete amplitude damping evolution, yielding the first experimental demonstration of this quite unconventional protocol. The quantum optics experiment that we have realized is based on the transmission of photon polarization qubits and has unambiguously proved the predicted entanglement recovery effect. The specific proof-of-principle demonstration has been constructed using combinations of amplitude-damping channels and unitary operations. However the proposed cut-and-paste technique is not limited to this scenario and can be applied also to more general single-qubit channels. We also envisage interesting generalizations of our approach to arbitrary multi-qubit channels [2] and to the physically important class of Gaussian entanglement-breaking channels [33, 34]. Our technique and its experimental realization demonstrates the real possibility of recover some amount of entanglement or extend its distance distribution over extremely noisy links, opening a novel opportunity towards the realization of quantum information networks of increasing complexity [35, 36]. Moreover, the unusual entanglement recovery effect studied in this work is also interesting in its own right and could open new research lines in quantum channel theory [2] and error correction protocols [18].

V. ACKNOWLEDGEMENTS

This work was supported by the ERC-Starting Grant 3D-Quest (3D-Quantum Integrated Optical Simulation; grant agreement no. 307783): <http://www.3dquest.eu>.

It was also partially supported by the ERC through the Advanced Grant n. 321122 SouLMan, and by PhD Chilean Scholarships CONICYT, "Becas Chile".

Appendix A: Amplitude Damping Channel

In the polarization basis $\{|H\rangle, |V\rangle\}$ the action of the AD map \mathcal{A}_η can be realized by means of the DIF of Fig. 5. Here an incoming signal $|\psi\rangle = a|H\rangle + b|V\rangle$ enters first a Sagnac Interferometer realized by means of a Polarizing Beam Splitter (PBS) which allows us to split the two polarization components by mapping them into two distinct optical paths, i.e. the black path **a** of Fig. 5 for the $|H\rangle$ component and the red path **b** for the $|V\rangle$ component, respectively. Accordingly the state of the signal immediately after the PBS can be expressed as $a|H\rangle \otimes |\mathbf{a}\rangle + b|V\rangle \otimes |\mathbf{b}\rangle$ where we expanded the Hilbert space by explicitly adding the path degree of freedoms. Inserting then a rotated HWP along **b** a rotation on the polarization degree of freedom of $|V\rangle \otimes |\mathbf{b}\rangle$ can then be induced while leaving the polarization of the $|H\rangle \otimes |\mathbf{a}\rangle$ unchanged, i.e. $|V\rangle \otimes |\mathbf{b}\rangle \rightarrow \sqrt{\eta}|V\rangle \otimes |\mathbf{b}\rangle + \sqrt{1-\eta}|H\rangle \otimes |\mathbf{b}\rangle$ and $|H\rangle \otimes |\mathbf{a}\rangle \rightarrow |H\rangle \otimes |\mathbf{a}\rangle$, the unitary operator responsible for such transformation being

$$U_0 \otimes |\mathbf{a}\rangle\langle\mathbf{a}| + U_{\alpha(\eta)} \otimes |\mathbf{b}\rangle\langle\mathbf{b}|, \quad (\text{A1})$$

where

$$\alpha(\eta) = \arccos(-\sqrt{\eta})/2, \quad (\text{A2})$$

and where for α generic U_α indicates the polarization rotation associated with a HPW element rotated by α , which in the basis $|H\rangle, |V\rangle$ is represented by the matrix

$$U_\alpha = \begin{bmatrix} \cos(2\alpha) & \sin(2\alpha) \\ \sin(2\alpha) & -\cos(2\alpha) \end{bmatrix}, \quad (\text{A3})$$

(as indicated in the Fig. 5 an unrotated HWP, performing the unitary transformation U_0 in Eq. (A1), was also inserted in the path **a** in order to preserve the temporal coherence between the two counter-propagating beams). Subsequently, on their second encounter with the PBS, the two signals enter an unbalanced Mach-Zehnder interferometer which separates the horizontal component of the **b** path adding to it a random phase $e^{i\omega}$ before recombining the signals at a 50% Beam Splitter (BS). Accordingly, with probability 1/2 the state emerging from the output port of the figure is described by the vector $|\psi\rangle_{out} = (a + e^{i\omega}b\sqrt{1-\eta})|H\rangle + b\sqrt{\eta}|V\rangle$ which, upon averaging over the random term ω , corresponds to the action of \mathcal{A}_η on $|\psi\rangle$, no photon emerging otherwise (in writing $|\psi\rangle_{out}$ the path degree of freedom have been removed since the BS is effectively filtering out one of them).

In the experimental setting shown in Fig. 3 the above transformation is iterated three times in order to reproduce the sequences of the maps Ψ and Φ as

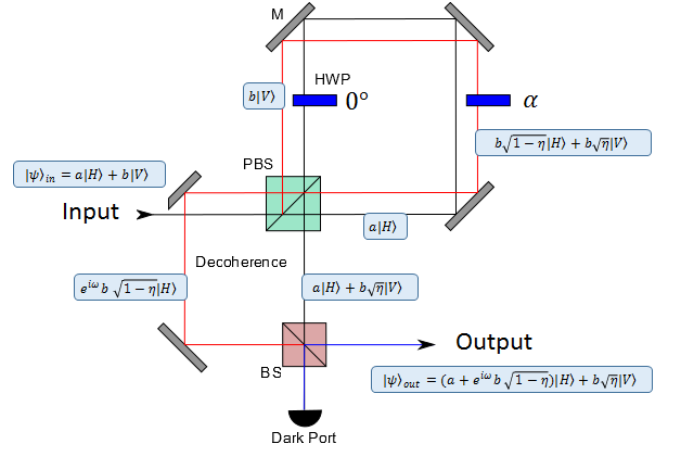


FIG. 5: Scheme of the experimental implementation of the AD map \mathcal{A}_η via a DIF loop. In this picture the path **a** associated with the $|H\rangle$ polarization component is indicated in black, while the path **b** associated with the $|V\rangle$ component is in red. The blue elements of the figure represent HPW elements.

detailed in the main text, with the precaution of setting the physical dimensions of the associated Mach-Zehnder interferometers to be different from each other in order to avoid any spurious coherence among the random phases they are meant to introduce.

Appendix B: Simulation of the scheme

The complexity of the geometry and the difficulties of coupling many spatial modes within one final single-mode fiber affect the entanglement preservation even if the maps implemented by the various DIF were set to operate as identity channels (i.e. taking $\eta_1 = \eta_2 = 1$ in Eq. (12) which implies setting $\alpha_1 = \alpha_{2,1} = \alpha_2 = 0$, and physically removing the HWPs implementing the unitary rotations \mathcal{U}_φ and \mathcal{U}_θ). Indeed, under such experimental conditions, the mean entanglement degradation on each DIF was greater than 1.3%, thus the maximum concurrence at end of the entire sequence of channels decreases from 98% to 94%. Besides the decrease of entanglement, the number of coincidences/sec was also affected, considering that the effective photon transmission of each double interferometer was $\approx 1/3$. Furthermore the effective operation of each interferometer, and therefore of each channel, can differ considerably from the others, even for small differences of the optical elements.

The numerical simulations presented in Fig. 4 have been obtained by taking into account all these imperfections. In particular we consider as input of the setup an effective input state of Werner form $\rho_{SA} = W|\Omega\rangle_{SA}\langle\Omega| + (1-W)\mathbb{I}_{SA}/4$ with the parameter $W \in [0, 1]$ extrapolated from the degree of entanglement of the source. Regarding the BS transformations instead we described them as

the following 2×2 matrices with respect to the spatial degree of freedom associated with the input ports,

$$BS = \begin{bmatrix} \sqrt{T'} & i\sqrt{R'} \\ i\sqrt{R'} & \sqrt{T'} \end{bmatrix}, \quad (\text{B1})$$

where the measured optical transmissivity T and reflectivity R have been renormalized to include losses $L = 1 - T - R$ by setting $T' = T/(1 - L)$ and $R' = R/(1 - L)$ (the average values of our set of BSs being $T = 0.48, R = 0.44$ and $L = 0.08$). Analogously to simulate the PBSs, we separated the action of each one of them in two BS-like operations, one for horizontally polarized light and one for vertically polarized light, i.e. adopting the notation introduced in (A1), we describe them in terms of the following unitary transformation

$$|H\rangle\langle H| \otimes BS_H + |V\rangle\langle V| \otimes BS_V. \quad (\text{B2})$$

Here BS_H and BS_V are operators coupling the vectors $|\mathbf{a}\rangle, |\mathbf{b}\rangle$ as in (B1) with normalized transmissivities T'_H, T'_V and reflectivities R'_H, R'_V , connected with the corresponding optical values $T_H, T_V, R_H,$ and R_V via the associated losses L_H and L_V . These parameters have been characterized sperimentally by using a CW diode laser with the same wavelength (810nm) of the expected entangled photons, obtaining on average over the set of the PBSs employed in the experiment, the values $T_H = 0.965, R_H = 0.0185$ and $L_H = 0.022$ ($T_V = 0.004, R_V = 0.948$ and $L_V = 0.048$).

In Fig. 6 we report a comparison between the ideal theoretical behaviour of the output concurrences C and the corresponding simulated values obtained by rescaling the setup parameters as detailed above. Apart from exhibiting degraded values of C , one notices that the simulated values present a clear difference in the behaviour of \mathcal{M}_1 and \mathcal{M}_2 and a crooked asymmetry in the concurrence peaks of \mathcal{M}' which are not present in the ideal theoretical curves but which are clearly evident in the experimental data of Fig. 4. The residual disagreement between the latter and the simulations must be attributed to the different fiber coupling efficiencies of all the 27 possible polarization-path modes which are difficult to chart due to mechanical random fluctuations of the setting.

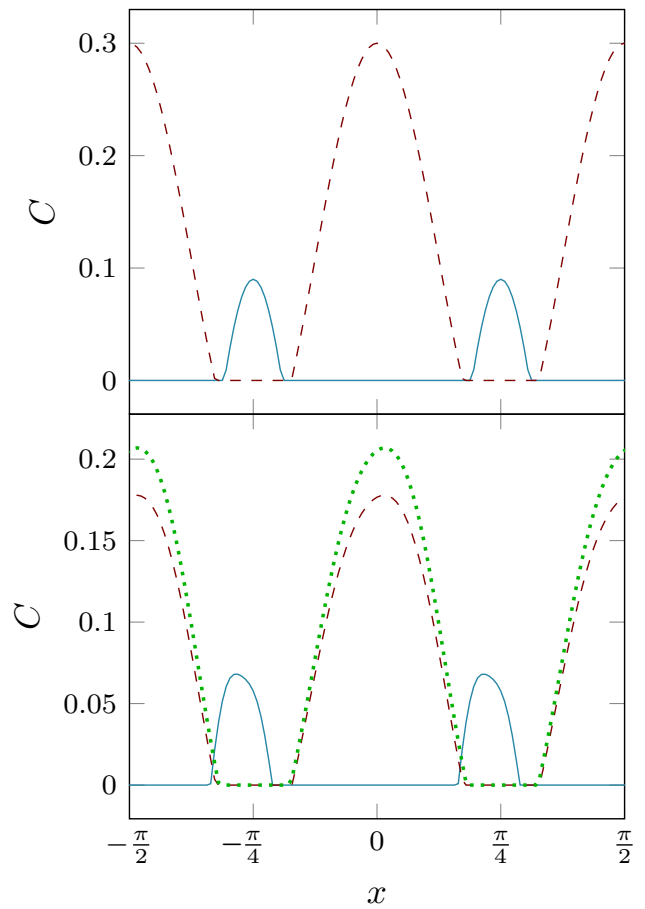


FIG. 6: **Top:** Concurrence values at the output of the scheme of Fig. 3 obtained assuming ideal conditions. The blue curve gives C for the map $\mathcal{M}' = \Phi \circ \Psi \circ \Phi \circ \Psi$ of Eq. (12) obtained by rotating the angle $x = \theta$ with φ fixed at $\frac{\pi}{4}$; the red-dashed curve represents instead the value of C for the channels $\mathcal{M}_1 = \Phi \circ \Phi$ or $\mathcal{M}_2 = \Psi \circ \Psi$, obtained by rotating the angle $x = \theta$ or $x = \varphi$ respectively. **Bottom:** Same plots as the Top section obtained by using real optical-elements simulations. Also in this case the blue curve represents \mathcal{M}' obtained by rotating the angle $x = \theta$ with φ fixed at $\frac{\pi}{4}$; the red-dashed curve represents instead \mathcal{M}_1 , obtained by rotating the angle $x = \theta$ while the the green-dotted curve represents \mathcal{M}_2 , obtained by rotating the angle $x = \varphi$. All the curves have been produced by taking the transmission coefficients of the active AD channels equal to $\eta = 0.3$.

-
- [1] J. P. Gordon, Proc. IRE 18981908 (1962).
 [2] A. S. Holevo, *Quantum Systems, Channels, Information. A Mathematical Introduction*, (De Gruyter, Berlin/Boston, 2012).
 [3] M. A. Nielsen, and I. L. Chuang, *Quantum computation and quantum information*, (Cambridge university press, Cambridge, 2010).

- [4] H. J. Kimble, Nature **453**, 1023 (2008).
 [5] L. M. Duan, M. D. Lukin, J. I. Cirac, and P. Zoller, Nature **414**, 413-418 (2001).
 [6] C. M. Caves, P. B. Drummond, Rev. Mod. Phys. **66**, 481537 (1994).
 [7] C. H. Bennett, G. Brassard, C. Crépeau, R. Jozsa, A. Peres, and W. K. Wootters, Phys. Rev. Lett. **70**, 1895

- (1993).
- [8] N. Gisin, G. Ribordy, W. Tittel, and H. Zbinden, *Rev. Mod. Phys.* **74**, 145 (2002).
- [9] A. Serafini, S. Mancini, and S. Bose, *Phys. Rev. Lett.* **96**, 010503 (2006).
- [10] R. Horodecki, P. Horodecki, M. Horodecki, and K. Horodecki, *Rev. Mod. Phys.* **81**, 865 (2009).
- [11] C. H. Bennett, G. Brassard, S. Popescu, B. Schumacher, J. A. Smolin, and W. K. Wootters, *Phys. Rev. Lett.* **76**, 722 (1996).
- [12] H. J. Briegel, W. Dür, J. I. Cirac and P. Zoller, *Phys. Rev. Lett.* **81**, 5932 (1998).
- [13] N. Sangouard, C. Simon, H. de Riedmatten, and N. Gisin, *Rev. Mod. Phys.* **83**, 33 (2011).
- [14] M. Horodecki, P. W. Shor and M. B. Ruskai, *Rev. Math. Phys.* **15**, 629 (2003).
- [15] A. S. Holevo, *Russian. Math. Surveys* **53**, 1295 (1999).
- [16] P. W. Shor, *Phys. Rev. A* **52**, R2493 (1995).
- [17] A. M. Steane, *Proc. R. Soc. London A* **452**, 2551 (1996).
- [18] B. M. Terhal, *Rev. Mod. Phys.* **87**, 307 (2015).
- [19] T. Yu, J. H. Eberly, *Quantum Inf. Comput.* **7**, 459-468 (2007).
- [20] P. Zanardi and M. Rasetti, *Phys. Rev. Lett.* **79**, 3306 (1997).
- [21] D. A. Lidar, I. L. Chuang and K. B. Whaley, *Phys. Rev. Lett.* **81**, 2594 (1998).
- [22] L. Viola and S. Lloyd, *Phys. Rev. A* **58**, 2733 (1998).
- [23] L. Viola and E. Knill, *Phys. Rev. Lett.* **94**, 060502 (2005).
- [24] S. Damodarapur, M. Lucamarini, G. Di Giuseppe, D. Vitali and P. Tombesi, *Phys. Rev. Lett.* **103**, 040502 (2009).
- [25] M. J. Biercuk, H. Uys, A. P. VanDevender, N. Shiga, W. M. Itano, and J. J. Bollinger, *Nature* **458**, 996 (2009).
- [26] A. Orioux, A. D'Arrigo, G. Ferranti, R. Lo Franco, G. Benenti, E. Paladino, G. Falci, F. Sciarrino and P. Mataloni, *Sci. Rep.* **5** 8575 (2015).
- [27] A. De Pasquale and V. Giovannetti, *Phys. Rev. A* **86**, 052302 (2012).
- [28] L. Lami and V. Giovannetti, *J. Math. Phys.* **56**, 092201 (2015).
- [29] R. Alicki, K. Lendi, *Quantum Dynamical Semigroups and Applications*, (Berlin, 1987).
- [30] H. P. Breuer, F. Petruccione, *The Theory of Open Quantum Systems*, (New York, 2002).
- [31] W. K. Wootters, *Phys. Rev. Lett.* **80**, 2245 (1998).
- [32] A. Fedrizzi, T. Herbst, A. Poppe, T. Jennewein and A. Zeilinger. *Opt. Express* **15**, 23 (2007).
- [33] A. S. Holevo, *Probl. Inf Transm. (Engl. Transl.)* **44**, 3 (2008).
- [34] A. De Pasquale, A. Mari, A. Porzio, and V. Giovannetti, *Phys. Rev. A* **87**, 062307 (2013).
- [35] L. M. Duan and C. Monroe, *Rev. Mod. Phys.* **82**, 1209 (2010).
- [36] S. Ritter, C. Nölleke, C. Hahn, A. Reiserer, A. Neuzner, M. Uphoff, M. Mücke, E. Figueroa, J. Bochmann and G. Rempe, *Nature* **484**, 195 (2012).